

<sup>1</sup> **Complicated reflection of linear internal tides from the Tasman continental  
2 slope**

<sup>3</sup> **JODY M. KLYMAK, \***

*The University of Victoria, Victoria, Canada*

<sup>4</sup> Harper L. Simmons and Dmitry Braznikov

*Affiliation, City, State/Province, Country*

<sup>5</sup> Samuel Kelly

*Affiliation, City, State/Province, Country*

<sup>6</sup> Jennifer A. MacKinnon, Matthew H. Alford, and Robert Pinkel

*Affiliation, City, State/Province, Country*

<sup>7</sup> Jonathan D. Nash

*Affiliation, City, State/Province, Country*

---

\* Corresponding author address: Jody Klymak, University of Victoria, Victoria, BC, Canada

E-mail: jklymak@uvic.ca

## ABSTRACT

9 The reflection of a low-mode incident internal tide on the Tasman continental slope is investigated using  
10 simulations of both the real topography, and simplified topographies. The majority of the slope is super-  
11 critical to the internal tide, but the response to the slope is complicated by a number of factors. The  
12 incoming beam is confined in space, it impacts the slope at an angle, there is a roughly cylindrical rise  
13 directly offshore of the slope, and a slope-mode wave is excited. These effects are isolated in simulations that  
14 significantly simplify the topography. Determining a reflected signal from an incident one is non-trivial, even  
15 in a numerical model, and the technique used here is to remove the reflector from the simulation and subtract  
16 an incident response from the total response to arrive at a reflected signal. Overall, the real slope reflects  
17 approximately 65% of the mode-1 internal tide as a mode-1 signal, which is less than two-dimensional linear  
18 calculations would predict, likely due to three-dimensional concavity of the topography. It is also less than  
19 recent glider estimates due to along-slope inhomogeneity. A synthetic three-point mooring array can predict  
20 almost any reflectivity because of spatial inhomogeneity. The Tasman Rise serves to diffract the incoming  
21 tidal beam into two beams, one focused downstream, and one diffracted to the north, with a substantial  
22 null in incoming energy between them. Along-slope heterogeneity is further enhanced by a partially trapped  
23 super-inertial slope wave that propagates along the continental slope, removing energy from the internal  
24 tide in some spots and re-radiating it further north. This wave is present even in a simplified straight-shelf  
25 topography.

## **26 1. Introduction**

27 Energy is lost from the surface tide when it interacts with topography, and in the deep ocean is largely  
28 redistributed as an internal tide. The fate of the internal tide is unclear, but surely depends on the dominant  
29 wavelengths that are forced. Gentle topography that is subcritical to the internal tide is likely dominated by  
30 higher vertical modes and is thought to break via wave-wave interactions relatively close to the topography  
31 (i.e. Polzin 2009; St. Laurent and Garrett 2002). However, steeper supercritical topography, while exhibiting  
32 significant local dissipation, tends to radiate a large fraction of the internal tide away from the topography as  
33 low-mode waves (i.e. at Hawaii Klymak et al. 2006; Carter et al. 2008). Given that a significant fraction of  
34 the internal tide energy is generated at steep topography (Legg and Klymak 2008), and that the distribution  
35 of the mixing it eventually drives has impacts on understanding the distribution of ocean properties and the  
36 strength of the overturning circulation (i.e. Melet et al. 2013), it is desirable to understand where and how  
37 this energy breaks.

One candidate sink for the low-mode internal tide is reflection and scattering from continental slopes. These slopes are known to be hotspots of turbulent mixing from the few observational studies to date (Nash et al. 2007; Klymak et al. 2011; Martini et al. 2013). However, these studies have also demonstrated some of the difficulties in tracking internal tide energy on these slopes. Net internal-tide fluxes are relatively straight forward to measure, but ideally we would like to separate the incident and reflected fluxes if a parameterization of turbulence on the slope is to be made since the incident fluxes are what drive the turbulence. The reflectivity of a continental slope is basically the ratio of the energy flux convergence divided by the total incident flux:

$$R = \frac{F_{out}}{F_{in}},$$

38 where  $F$  is depth integrated for a two-dimensional budget or line-integrated for a three-dimensional one.  
39 Even simple two-dimensional linear models of reflection indicate that determining the reflectivity will be  
40 challenging, with reflection co-efficients strongly depending on the modal content and phases of the incident  
41 internal tides (Klymak et al. 2011) and the local surface tide (Kelly and Nash 2010). These linear models  
42 have been used globally to estimate reflection co-efficients for the mode-1 tides on realistic continental slope  
43 bathymetries, (Kelly et al. 2013a,b), but these calculations assume the incoming tide is known, and that the

44 slope is relatively homogenous over a long distance (presumably the mode-1 wavelength).

45 Determining the incident flux,  $F_{in}$ , from field data, and even from a numerical model with sufficient  
46 complexity, is not trivial. In two dimensions, or with simple plane wave geometries, it is relatively easy to  
47 fit incident and reflected plane waves and recover the desired reflection co-efficient (figure 1a). In the real  
48 ocean, even if the tidal components can be easily separated from confounding influences, internal tides are  
49 often spatially inhomogeneous, and form lateral “beams” (in x-y) that make plane wave fits difficult from a  
50 finite array of moorings; for instance the mooring array could be located more in the incoming beam than  
51 the reflected, leading to an exaggeration of the dissipation (figure 1b). Plane-wave fits to satellite altimetry  
52 tracks are promising, but will also suffer from a lack of fidelity if the internal tides are inhomogeneous on  
53 the scale of the plane wave fits (Zhao and Alford 2009). In the model, high resolution temporal and spatial  
54 information makes it possible to separate signals spectrally according to their direction of propagation (i.e.  
55 using a Hilbert transform Mercier et al. 2008), but this method works best if there are no boundaries and the  
56 signals at the edges of the model domain can be tapered to reduce leakage, neither of which are applicable  
57 here.

58 The region considered here is the Tasman continental slope, and is the focus of a concentrated internal  
59 tide experiment. As preliminary work, it has been sampled continuously by gliders for many months in 2012  
60 and 2013 (Johnston et al. 2015). The gliders were flown to form internal waves antennae over which internal  
61 plane-wave fits were made. These efforts show a clear standing wave pattern, with amplitudes and phases  
62 as one would expect for internal waves incident on the slope from the southeast where internal tides are  
63 expected to be generated from the Macquarie Ridge (figure 2a). The amplitudes of the interfering waves  
64 were such that the reflectivity is predicted to be high on this slope, with estimates of 0.7 to 1. from the  
65 arrays (Johnston et al. 2015). The gliders also picked up a 100-km wavelength wave propagating along slope  
66 towards the north, a finding we isolate and discuss below.

67 Here we run numerical simulations that are meant to represent a mode-1 internal  $M_2$  tide incident on  
68 the Tasman Slope, east of Tasmania. The simulations are only forced by this incident internal tide, and  
69 there is no local forcing, allowing the effect of the reflection to be isolated. After discussing the model setup  
70 section 2, we briefly consider the response this forcing has on the slope section 3 and compute and energy

71 budget of the complete response. In order to separate the physics of the reflection, we then simplify the  
72 geometry section 4, both geometrically, and by removing parts of the topography. This technique allows us  
73 to separate incident and reflected signals from the total response without appeal to simplified wavefits. We  
74 end with a discussion of the results (section 5) and a summary (section 6).

## 75 2. Model setup

### 76 a. Basics

77 The numerical model used here is the MITGCM (Marshall et al. 2006). The setup is very similar  
78 to Buijsman et al. (2014), with the model run in hydrostatic mode, background (isotropic) diffusivities  
79 and viscosities of  $10^{-5} \text{ m}^2 \text{s}^{-1}$ , and enhanced diffusivity and viscosity in regions of temporarily unstable  
80 stratification, as in Klymak and Legg (2010). A second-order flux-limiting temperature advection scheme  
81 is used which results in some numerical dissipation and diffusion. Tests were run with weaker forcing, and  
82 the fraction of energy dissipated did not change, indicating that the dissipation highlighted below is heavily  
83 influenced by numerical dissipation due to the lack of lateral resolution. Dissipation is not the main focus  
84 of this paper, and finer resolutions have been used for more focused efforts dealing with turbulence on the  
85 slope.

86 Topography is from a data set that combines Smith and Sandwell (1997) and multibeam data from  
87 Australian surveys (Whiteway 2009) (figure 2b). For this paper, we use a cartesian co-ordinate system  
88 centered at 44S, 148 E, with  $y$  pointing 12 degrees east of geographic north (magenta lines figure 2). This  
89 co-ordinate system is close to cross-slope in the x-direction, and is used for conceptual convenience. The  
90 simulations are run on a f-plane ( $f = -10^{-4} \text{ s}^{-1}$ ), so no planetary beta effect has been included.

91 Relatively high lateral resolution is used along the continental slope (figure 3a, smallest inset green box)  
92 of  $\delta x = \delta y = 1 \text{ km}$ . Resolution is expanded by 3.5% per grid cell beyond the high-resolution region, to a  
93 maximum of 5 km in the second largest inset box (figure 3a); this keeps the resolution over the Tasman Rise  
94 and the rest of the continental slope at least 5 km. Further out, the grid spacing is again increased at 3.5%  
95 per grid cell until a maximum grid cell size of 10 km is reached.

96 Vertical resolution is approximately stretched so  $dz \sim N$ , where  $N^2(z) = -\frac{g}{\rho_0} \frac{d\rho}{dz}$  is the vertical stratification.  
 97 200 vertical grid cells are used for these simulations. The vertical stratification is from the World  
 98 Ocean Atlas for the Tasman Sea just offshore of Tasmania (Boyer et al. 2013), and is assumed laterally  
 99 constant in the domain. This precludes any mesoscale effects, which are believed to be important in this  
 100 area, and are the subject of future work.

101 *b. Forcing*

102 To simplify the generation problem we apply an analytical forcing to our model. This is composed of  
 103 two line sources at approximately the location of the Macquarie Ridge (figure 3a). The initial conditions  
 104 and the southern and eastern boundaries of the model were set with this forcing. The forcing is based on  
 105 (Rainville et al. 2010), except instead of a single point source placed a distance  $R$  from the line source, the  
 106 line source is digitized as a number of discrete point sources and their response in the domain summed. The  
 107 mode-1 pressure anomaly is given by:

$$p'(x, y, t) = \sum_{i=1}^N a_i \exp(j(|k_t|r_i - \omega t)) \quad (1)$$

108 where  $r_i = \sqrt{(x - x_i)^2 + (y - y_i)^2}$  is the distance to the source, and  $|k_t|$  is the absolute value of the mode-1  
 109 wavenumber:

$$k_t = \frac{(\omega^2 - f^2)^{1/2}}{c_e} \quad (2)$$

110 where  $\omega$  is the frequency of the tide,  $f$  is the Coriolis frequency, and  $c_e$  is the eigenspeed of the vertical mode  
 111 equation:

$$\frac{d}{dz} \left( \frac{1}{N^2} \frac{d\psi}{dz} \right) + \frac{1}{c_e^2} \psi(z) = 0. \quad (3)$$

112 Here  $\psi(z)$  is the eigenfunction that sets the shape of the vertical mode, and the boundary conditions are  
 113  $d\psi/dz = 0$  at  $z = 0$  and  $z = -H$ , where  $H$  is the water depth. For convenience, we normalize  $\psi_m(z)$  so that

$$\int_{-H}^0 \psi_m^2(z) dz = 1. \quad (4)$$

114 Horizontal velocities can be linearly decomposed by these shapes, as can the pressure signal; vertical veloci-  
 115 ties, and displacements are decomposed by the derivative of the normalized  $\psi_m$ :  $d\psi_m/dz$ .

116 To compute the wavefield, the horizontal velocity components are derived from the internal wave consis-  
 117 tency relations:

$$u(x, y, t) = \sum_{i=1}^N \frac{k_x \omega + j k_y f}{\omega^2 - f^2} \frac{p'_i}{\rho} \quad (5)$$

$$v(x, y, t) = \sum_{i=1}^N \frac{k_y \omega - j k_x f}{\omega^2 - f^2} \frac{p'_i}{\rho} \quad (6)$$

118 where  $k_x = k_t \cos(\theta_i)$  and  $k_y = k_t \sin(\theta_i)$  are calculated from the angle to each element of the line sources  
 119  $\theta_i = \arctan((y - y_i)/(x - x_i))$ .

120 The resulting incoming wavefield (figure 3a) has a beam of energy flux that radiates northwest, and is  
 121 relatively tightly focused. The interference pattern creates a null to the south and north, and a secondary  
 122 beam that radiates due west. This schematic agrees with more realistic regional tidal models (H. Simmons,  
 123 in preparation), and the amplitude of the beam was tuned to give approximately  $7 \text{ kW m}^{-1}$  of flux incident  
 124 at Tasmania in the pictured realization. Most runs below were scaled to have weaker (more linear) fluxes,  
 125 with approximately  $2 \text{ kW m}^{-1}$  at Tasmania, but exactly the same spatial pattern. The initial condition is  
 126 applied uniformly through the domain, regardless of bathymetry, so there are some start-up transients as  
 127 the proper baroclinic flow develops.

128 This forcing is applied on the eastern and southern boundaries of the domain. The northern and western  
 129 boundaries are sponges where the velocity is slowly dropped to zero and the stratification relaxed to the  
 130 initial stratification (figure 3a, green rectangles). Our main focus is the area from  $y=0$  to 400 km, so the  
 131 boundaries are sufficiently far that small residual reflections do not affect the response.

132 The ideal response off the Tasman topography would be as a plane-wave reflection from a wall at  $x = 0 \text{ km}$   
 133 (i.e. Johnston et al. 2015). Here we have a relatively confined beam, but we can make a start by considering  
 134 the reflection the beam from a wall at  $x = 0 \text{ km}$  for  $y > 0 \text{ km}$  (figure 3b,c) using the method of images  
 135 with identical line sources mirrored about the  $y$ -axis, and their phase shifted by 180 deg. The reflection  
 136 pattern that sets up is not entirely regular, but has some straight-forward features. The incoming beam  
 137 impacts the wall at approximately 30 deg. The horizontal wavelength of an  $M_2$  internal tide is 178 km, so  
 138 the standing wave in the x-direction will have a wavelength  $178/\cos(30) \approx 200 \text{ km}$  and in the y-direction  
 139 will have a wavelength of approximately 350 km. These spatial scales are readily apparent in the analytical

140 forcing despite the non-plane-wave character of the idealized forcing (figure 3c). Note that the standing  
141 energy flux (figure 3b) has peaks and nulls in absolute value, with the peaks having large flux to the north.  
142 The peaks are every half cross-slope wavelength (i.e. 100 km). The nulls have weak southward energy flux  
143 (though it is difficult to discern from the subsampled arrows in the plot).

### 144 3. Realistic model simulation

145 The response of the forcing in the most complex domain motivates the more idealized experiments that  
146 follow. From the initial forcing (figure 4a), a complex wavefield develops with clear scattering from the  
147 Tasman Rise, the shelf, and numerous small inhomogeneities on the sea floor (figure 4b–d). Looking along  
148 shelf, the phase of the velocity signal can be seen changing approximately every 200 km, and it changes  
149 approximately every 100 km offshore.

150 This sets up a complicated interference pattern that shows inconsistent cross-slope fluxes and peaks and  
151 nulls in the along-slope fluxes to the north, as we might expect from an oblique standing wave (compare  
152 figure 4h to figure 3b). However the pattern is complicated, with offshore peaks at approximately the correct  
153 spacing offshore, but not lining up precisely in the north-south direction. There are inhomogeneities in the  
154 energy that are not accounted for by a simple two-wave model.

155 An energy balance is performed on the model using the terms outlined in Kang and Fringer (2012); Kang  
156 (2011). Their energy balance vertically integrated can be schematicized as:

$$dE_{bc}/dt = -\nabla_H \mathbf{F}_{bc} + \text{Conversion} - \text{Dissipation}. \quad (7)$$

157 where  $E_{bc}$  is the depth-integrated baroclinic energy density,  $\mathbf{F}_{bc}$  is the depth integrated energy flux, including  
158 both the pressure work term and the non-linear advection of energy (which is small in our runs). “Conver-  
159 sion” is a complex term representing transfer from barotropic motions to baroclinic (Kang 2011, eq. 5.102)  
160 and includes the barotropic heaving of the water column, the density anomaly, and a non-linear horizontal  
161 advection term. The non-linear terms can be non-trivial in real bathymetry (Buijsman et al. 2014). The con-  
162 version term is positive if the barotropic tide loses energy and the baroclinic tide gains energy. “Dissipation”  
163 is computed here as the residual, and includes dissipation due to interior viscosity, numerical dissipation,

164 bottom drag, and diffusion of energy (small).

165 Of note in the energy calculation is that the largest local term in the energy budget is an alternating  
166 pattern of barotropic-baroclinic conversion at the shelf break balanced by baroclinic flux convergences and  
167 divergences (figure 5). The importance of the barotropic-baroclinic term can also be seen by considering the  
168 x-integral of the energy budget from  $x = -50$  km to  $+100$  km (figure 6). Recall that the simulations have  
169 no barotropic forcing. This coupling is catalyzed by a start-up transient hitting the slope with the incoming  
170 internal tide beam, and continues throughout the simulation, and is probably a leaky super-inertial slope  
171 wave (see section 5).

172 The time series of the energy terms integrated along the shelf demonstrates that the barotropic-to-  
173 baroclinic term is relatively small when averaged, with a small loss of energy from the baroclinic tide to the  
174 barotropic in the integral region (figure 6b). The model is largely in a steady state by tidal cycle 15, with  
175 some residual oscillations in  $dE/dt$  and the flux convergence. The large-scale baroclinic energy changes do  
176 not change the dissipation residual very much, which is relatively constant after 5 tidal cycles. To put the  
177 50 MW of dissipation into context, the initial energy that comes in the east and south sides of this analysis  
178 box in the initial conditions is 315 MW, so the model is dissipating about 17% of the incoming energy.  
179 However, note that the dissipation is not the focus of these model runs nor of this paper. The forcing here  
180 is approximately a factor 3 lower than the real forcing, so its likely the fraction of dissipation at this site is  
181 higher (probably closer to 25%) if real forcing is used.

182 The majority of the energy budget is in the first vertical mode (figure 6c). Net fluxes in the region directly  
183 offshore of the shelf break ( $0 < x < 80$  km, and  $0 < y < 400$  km) are composed of substantial mode-1 energy  
184 converging on the shelf (95 MW net), and some reflected energy escaping in higher modes (28.3 MW, mostly  
185 in modes 2–4). The 95 MW net flux is made up of the incoming and reflected mode-1 energy, and separating  
186 those fractions out is the subject of the next section. There is some incoming higher-mode energy as well  
187 due to scattering from the Tasman Rise, but as we will also show below, this is minor. The spatial pattern  
188 (not shown) of the mode conversion at the continental slope indicates hot-spots for conversion. Modes 2 and  
189 4 have a hotspot of conversion near  $y = 250$  km, and Mode 3 at  $y = 325$  km.

## 190 4. Simplified geometries

191 To help tease apart the effects of the Tasman Rise and the non-uniform shelf, we carry out a few simplified  
192 geometric experiments (figure 7;figure 8). The REAL case is the one discussed above (figure 8f). The NO  
193 TOPO case has no topography at all (figure 8a), just the beam being forced at the south and east boundaries  
194 and (mostly) absorbed at the west and north. RISE was run with the real bathymetry west of  $x = 70$  km  
195 (figure 8e). Three idealized geometries simplify the physics even more: the SHELF case has a supercritical  
196 two-dimensional continental shelf running north from  $y = 0$  km(figure 8d). ROUND RISE is a 1700-m tall  
197 cylinder-shaped bump with radius of 50 km centered at approximately the same location as the Tasman Rise,  
198 with no shelf to the west (figure 8b). The simplified shelf and the rise are both used in the SHELF/RISE case  
199 (figure 8c).

### 200 a. Shelf-only configuration

201 The simplest topography is the SHELF configuration (figure 8d). Here we have a response that is quite  
202 similar to the analytical response calculated above (figure 3b). The only difference between these two cases  
203 is the narrow shelf west of  $x = 0$  km and the slight slope to the continental slope. The interference pattern  
204 between the incoming wave and the reflected wave is clear in this plot, with the same characteristic length  
205 scales as above, and a slight bending of the response due to the radial spreading of the beam.

206 The goal of this paper is to determine the amount of reflectivity of the continental slope. This is a hard  
207 number to determine in a complicated geometry, and naturally depends on the region of integration. For  
208 the SHELF configuration the situation is relatively simple, and we use it to illustrate the numerical technique  
209 used below. The signal in the full simulation is assumed to consist of an “incoming” signal and a reflected  
210 signal, so we can decompose the east-west velocity amplitude of the first vertical mode (for example) as:

$$u_1^t(x, y) = u_1^i + u_1^r \quad (8)$$

$$v_1^t(x, y) = v_1^i + v_1^r \quad (9)$$

$$p_1^t(x, y) = p_1^i + p_1^r \quad (10)$$

211 where  $u_1^t$  is the complex amplitude of the  $M_2$ , mode-1 east-west velocity of the simulation with the reflection,

<sup>212</sup>  $u_1^i$  of the incoming signal, and  $u_1^r$  of the reflected signal. We assume for this example that the incoming  
<sup>213</sup> signal  $u_1^i$  is given by the No TOPO simulation, and  $u_1^t$  is from the SHELF simulation. The reflected signal  
<sup>214</sup>  $u_1^r$  is simply the difference of these two.

<sup>215</sup> In order to compute and energy budget, we consider that the energy fluxes are calculated from the  
<sup>216</sup> decomposed signals as:

$$P_{u1}^t = u_1^t p_1^t \quad (11)$$

$$= \underbrace{u_1^i p_1^i}_{\text{Incoming}} + \underbrace{u_1^r p_1^r}_{\text{Reflected}} + \underbrace{u_1^i p_1^r + u_1^r p_1^i}_{\text{Cross Terms}} \quad (12)$$

$$P_{v1}^t = v_1^t p_1^t \quad (13)$$

$$= \underbrace{v_1^i p_1^i}_{\text{Incoming}} + \underbrace{v_1^r p_1^r}_{\text{Reflected}} + \underbrace{v_1^i p_1^r + v_1^r p_1^i}_{\text{Cross Terms}} \quad (14)$$

<sup>217</sup> The cross terms are not negligible for any realistic forcing, and indeed give rise to the interference patterns  
<sup>218</sup> seen above, and is a consequence of rotation's influence on the internal waves (Nash et al. 2004; Martini  
<sup>219</sup> et al. 2007).

<sup>220</sup> The “total” response (figure 9d) consists of the incoming response (figure 9a), and the “reflected” signal  
<sup>221</sup> (figure 9b), and substantial cross-terms (figure 9c). The cross terms are mostly perpendicular to the direction  
<sup>222</sup> of reflection (i.e. perpendicular to the shelf) and alternate fluxing energy to the north and south every half  
<sup>223</sup> cross-shelf wavelength. Combined, these three components give the “total” flux with net fluxes to the north  
<sup>224</sup> in alternating peaks every full offslope wavelength.

<sup>225</sup> The reflected response (figure 9b) shows approximately what we would expect with energy being radiated  
<sup>226</sup> to the north-east. There is some concentration of this energy at  $y \approx 75$ km, and  $y \approx 225$ km. As above, this  
<sup>227</sup> is because of coupling with a slope wave that is strummed by the initial conditions. This coupling causes  
<sup>228</sup> a redistribution of the reflected energy, focusing it approximately every along-slope wavelength of the shelf  
<sup>229</sup> wave (we show below that this wavelength changes as the shelf geometry changes).

<sup>230</sup> Performing this analysis for the lowest 10 modes, we arrive at an energy budget for the shelf in the green  
<sup>231</sup> box in the figures ( $0 < y < 400$  km, and  $x < 80$  km; figure 9, inset budgets). Note that we assume the  
<sup>232</sup> flux through  $x = 0$  is zero. With this calculation, we see that 408 MW is incident on the shelf in mode-1.  
<sup>233</sup> There is also a net flux of 50 MW into this region from the cross terms. This is a redistribution of energy

234 from north of our box into the box. There is a net convergence of this cross-term energy because there is  
235 dissipation in the box; in a purely inviscid solution this term should balance to zero over a closed box. If we  
236 move the integration further north, the cross-term flux drops to zero.

237 Most of the incoming energy reflects back out of the box (figure 9b), with the bulk remaining in mode 1,  
238 and some scattering to higher modes due to the shelf. This scattered energy reflects to the north east (not  
239 shown). The mode-1 reflection is affected by a shelf wave that transfers energy to and from the barotropic  
240 tide along the slope, resulting in nulls and peaks in the mode-1 reflection.

241 *b. Tasman Rise only*

242 The Tasman Rise has a profound effect on the energy that impacts the continental slope, as well as  
243 having some back reflection (figure 8e and f). The incoming beam is almost 500 km wide at  $x = 0$  if there is  
244 no Tasman Rise, but breaks into three narrower beams when there is a Tasman Rise (figure 8e). Upstream  
245 of the rise, the effect is somewhat less energy propagating westward, with an interference pattern towards  
246 the east indicating some back reflection.

247 This pattern can be explained in terms of diffraction of the internal tide beam from a deep obstacle (i.e.  
248 Johnston and Merrifield 2003). There is a down-wave concentration of energy along the seamount's axis,  
249 a null, and sidelobes to the north and south. In this case, the incident beam is of comparable size to the  
250 obstacle, leading to an asymmetry, and a stronger lobe to the north than south.

251 Most of the response due to the Tasman Rise can be modeled simply as a cylindrical obstacle in the  
252 beam (figure 8b and c). Here our obstacle is 1800 m high in 5000 m of water, and has a radius of 50 km  
253 (figure 7). This captures most of the features of the actual Tasman Rise, despite not having a shallow spire  
254 in the center and being slightly smaller than the real Rise. The differences make the simplified response  
255 have weaker nulls and the whole response is directed a bit further north than the real Rise. Adding the shelf  
256 (figure 8c) yields a response that bears substantial similarity to the REAL forcing case.

257 Decomposing into an incoming and reflected signal (figure 10) demonstrates the effect of the Tasman  
258 Rise on the response. Less energy is incident on the control volume, largely because the diffraction redirects  
259 some of that energy to the north of  $y = 400\text{km}$ . There is a strong reflection of energy where the main

260 diffraction lobe reflects from the slope (figure 10b), and a smaller maximum just to the north ( $y = 250\text{km}$ )  
261 due to the along-shelf wave that is strummed. There is a reflection further north where the northern lobe of  
262 the diffraction pattern reflects.

263 The incoming energy has some more higher mode content due to scattering at the cylindrical rise (fig-  
264 ure 10a), though it is still 95% mode-1. The reflection is almost 80% mode-1, with some scattering to higher  
265 modes. The net flux shows approximately 15% of the incoming energy is dissipated at the shelf.

266 *c. Real Case*

267 The REAL forcing is similar, if more complex (figure 11). The simulation using the bathymetry in the  
268 RISE ONLY case (figure 8e) is used as the “Incoming” energy flux, and the REAL (figure 8f) case is the  
269 “Total”. Compared to the cylindrical rise, the real Tasman Rise creates a sharper diffraction pattern, and  
270 more back reflection. However, the REAL simulation has many of the same features as the RISE AND SHELF  
271 simulation (figure 8c).

272 Slightly less incoming energy passes into the control volume (figure 11a) because the diffraction by the  
273 real Tasman Rise is sharper than the cylindrical rise. As for the cylindrical rise case, there is some incoming  
274 higher mode energy due to forward scattering, though again over 95% is mode-1. Reflection is concentrated  
275 near  $y = 125\text{ km}$  and  $y = 450\text{ km}$ , associated with the diffraction nodes, with about 85% in mode 1  
276 (figure 11b). Dissipation is less than 25% of the incoming energy (figure 11d).

277 **5. Discussion**

278 *a. Estimating reflection co-efficients*

279 A major goal of this effort is estimating the fraction of incoming tide that is reflected by the Tasman  
280 continental slope to come up with a reflectivity co-efficient  $R = F_{ref}/F_{in}$ . Even here we need to be careful  
281 to discriminate between the mode-1 reflection,  $R_1 = F_{ref,1}/F_{in,1}$ , and the total reflection into all the modes,  
282  $R_T = F_{ref}/F_{in}$ . Evaluating these co-efficients is less straightforward than it may sound because it is difficult

283 to separate the incoming from reflected signal in complicated geometry, even in a fully resolved numerical  
284 model, let alone in observations. Above, we used an integrated measure, comparing the incoming flux from  
285 a model with no continental slope to one with a continental slope and integrating the fluxes over a control  
286 volume from  $y = 0$  to 400 km. This was an arbitrary choice, but yielded reflectivities of  $R_1 = 0.65$  and  
287  $R_T = 0.76$  (figure 11).

288 Determining reflectivity from a mooring array is significantly complicated by three-dimensionality and  
289 along slope variability. From the mooring array in figure 11, the reflectivity is  $R_1 = 0.6/1.3 = 0.46$ , a  
290 significant under-estimate. The reason for this should be relatively clear from looking at figure 11a,b; the  
291 mooring array nicely captures the northward diffracted ray, but catches some of the reflected pattern from  
292 the main beam to the south. There are significant interferences in the reflected patterns (figure 11b) because  
293 the reflected pattern is a complicated superposition of the cylindrically spreading reflections along the slope.

294 Determining the reflectivity as a function of along-slope direction  $y$  is difficult. Simply lining up the  
295 onslope fluxes  $x$ -direction) does not yield useful results because the reflection from any given point on the  
296 slope radiates cylindrically, and it is necessary to integrate over volumes. Here we take the same approach  
297 as used in the previous section (i.e. figure 11), but integrate over smaller control volumes (80 km in  $y$ ) to see  
298 the reflectivity as a function of  $y$  (figure 12a,b). The incoming flux every 80 km shows the diffracted beam  
299 pattern with a maximum net incoming flux at  $y = 120\text{km}$  (figure 12a, red line) and a secondary peak to  
300 the north at about 440 km. The net reflectivity from these boxes ranges from 0.8 to a low of almost zero at  
301  $y = 280$  km (figure 12b, solid blue line). Note an uncertainty in the flux decomposition associated with the  
302 flux in the cross terms (figure 12a, purple line). This term does not balance to zero, and forms a significant  
303 part of the energy budget over such small control volumes. It cannot be uniquely decomposed into either  
304 the incoming or reflected energy terms, so remains as an uncertainty.

305 The fraction of the tide reflected into mode 1 (and higher) can be predicted from linear theory using  
306 the method described by Kelly et al. (2013b) of matching Laplacian tidal solutions at discrete steps on a  
307 discretized topography. In two-dimensions an oblique incidence to the tide can make a substantial difference  
308 in the modal distribution of the reflected tide (Kelly et al. 2013c). If we run these solutions for the Tasman  
309 Slope with an incident angle of 30 degrees, the reflectivity into mode-1,  $R_1$  is similar to the numerical

310 simulation (figure 12b, thick black line). The predicted reflectivity is greater for most of the ridge, but the  
311 null at  $y = 250$  km is captured.

312 To compare with the energy budget for the REAL simulation above, we can average the reflectivity from  
313 the linear model between  $y = 0$  and 400 km. A naive average yields  $R_1 = 0.71$ , however, that does not take  
314 into account the varying strength of the incoming diffracted beam, which is stronger where the reflectivity is  
315 higher. If we do that, the reflectivity averages  $R_1 = 0.8$ , and is substantially larger than  $R_1$  over this same  
316 region from the numerical simulation of  $R_1 = 0.65$ .

317 An attempt has been made to estimate reflectivity from this site from autonomous gliders surveys at  
318 this site a(Johnston et al. 2015). First, the gliders saw a substantial concentration of energy shoreward of  
319 the Tasman Rise. This is a feature of the model, and clearly explained by the diffraction of energy by the  
320 Tasman Rise (figure 11).

321 For the region in the lee of the Tasman Rise, Johnston et al. (2015) estimate a reflectivity of the mode-1  
322 internal tide of between 0.8 to 1.0 by fitting plane waves to the velocity and displacement amplitudes and  
323 phases. If we confine our incoming versus outgoing energy budget to the region  $80 \text{ km} < y < 200 \text{ km}$ ,  
324 representative of their *Spray 56* deployment, we calculate a reflectivity of 0.7, which is lower than their  
325 lowest estimate of 0.8, and much lower than their high estimate of 1.0. Their *Spray 55* deployment covered  
326 more of the slope (up to  $y = 300$  km). In this domain, they estimate a reflectivity of 0.6. This is in excellent  
327 agreement with the numerical simulation, which achieves exactly the same result from  $0 \text{ km} < y < 300 \text{ km}$ .

328 The directions of wave propagation fit from the glider data is not as well in agreement with the model.  
329 The fits to the *Spray 55* data show incoming energy at between 125 and 145 degrees, which is similar to  
330 the model. However the reflection is slightly south of due east (0 to -30 degrees geographic), whereas the  
331 numerical model is definitely to the north east far from shore. An explanation is evident from close inspection  
332 of figure 11b between the Tasman Rise and the continental slope. Here the off-shore energy flux is almost  
333 exactly in the x-direction, (-12 degrees geographic), in agreement with the glider observations.

334 Finally, one of the gliders (*Spray 56*) picked out a northward propagating disturbance along the conti-  
335 nental slope with wavelength of 100 km. This wavelength matches the wavelength of the slope wave seen in  
336 the real simulations (figure 5a,b). Interestingly, they only pick this wavelength out in vertical displacement

337 data, not in velocity.

338 *b. Slope wave importance and dynamics*

339 The structure of the barotropic-to-baroclinic conversion on the slope is an intriguing feature of these  
340 simulations, and appears in regional simulations (Simmons, in prep) and the glider data (Johnston et al.  
341 2015). Here, it shows up most clearly in the SHELF simulations because of the simplified bathymetry.  
342 However, it is also clear in the REAL simulation (figure 5a). This slope wave redistributes energy in the  
343 reflected baroclinic response (figure 9), taking a relatively homogenous incoming energy source and focusing  
344 the reflection every 200 km or so along shelf.

345 This wave is a slope mode that is strummed by the incident internal tide at the “corner” of the topography  
346 ( $x = 0, y = 0$ ); a long shelf without the corner does not excite this wave, nor does an internal tide  
347 coming directly from the east and hitting the topography at a normal angle. The along-slope wavelength is  
348 independent of the along-slope wavelength in the open water (tested by changing the angle of the incident  
349 tide), and is a robust feature of the shelf shape. Wider shelves have shorter along-slope wavelengths, and  
350 narrow shelves have longer (figure 13).

351 These waves are superinertial, and hence not traditional subinertial coastally trapped waves (i.e. Brink  
352 1991). However, Dale and Sherwin (1996) show that superinertial waves on continental slopes can still have  
353 modes that grow more rapidly in frequency and along-slope wavenumber. Here our frequency is fixed, so we  
354 expect there to be resonant along-slope wavenumbers. The vertical-cross slope response of these waves, or  
355 modes, are basically a local mode-1 in the deep ocean, and close to barotropic on the shallow shelf, matching  
356 our findings here.

357 These slope modes transfer energy from the mode-1 internal tide to the barotropic (in our local account-  
358 ing). Because the waves are super-inertial, they are not perfectly trapped on the slope, and require forcing to  
359 keep their energy, and re-radiate energy offshore. Calculating how much energy is redistributed as a function  
360 of the shelf-wave amplitude is an interesting problem that will require further research.

## 361 6. Summary

362 A mode-1 internal tide was launched at a variety of topographies representing the Tasmanian continental  
363 slope. The goal was to determine the “reflectivity” of this slope, in terms of the modal content of the  
364 reflected energy and the local dissipation. The latter is somewhat suspect in this model because of crude  
365 lateral resolution, but the REAL simulation indicated that 21% of the incoming energy was dissipated, and  
366 65% was reflected as mode-1 energy. The incoming internal tide flux used here was weak compared to the  
367 flux modeled and inferred from altimetry in the Tasman Sea, so we expect the dissipation in more strongly  
368 forced models to increase.

369 Despite a relatively simple incoming internal tide which is linear, semi-diurnal, and mode-1, we have  
370 found a rich and complex response of the topography when the remote wave impacts the topography east  
371 of Tasmania. The response can be characterized as follows:

- 372 • Diffraction of the beam by the Tasman Rise,
- 373 • oblique reflection from the continental slope,
- 374 • and a forced slope wave response that redistributes reflected internal energy along-slope.

375 Of these, perhaps only the second effect was expected before carrying out the simulations. However, as we  
376 saw above, even the reflection problem is significantly complicated in the presence of three-dimensionality,  
377 such that it is difficult to determine the appropriate slope for the incoming wave to impact the shelf.

378 Diffraction around underwater topography should have been expected, however, the relative depth of  
379 the obstacle makes it surprising that the effect is so strong. The fact that the size of the Tasman Rise is  
380 close to that of a wavelength of the incoming internal tide makes predicting the diffraction pattern difficult.  
381 Baines (2007) considers generation of internal tides at seamounts, but does not deal with scattering and  
382 diffraction. The problem is similar to electromagnetic waves passing through a wire, but a linear response  
383 for that problem is not trivial to compute (i.e. Bonod et al. 2005), and still does not have a confined vertical  
384 mode structure as we find in the internal wave problem.

385 The excitation of slope waves is a nice corroboration of theory by Dale et al. (2001), and it has a low-order  
386 effect on the redistribution of energy along slope. If the dissipation in this crude model is to be believed (and

387 we feel it is actually close, based on higher resolution runs), the redistribution affects where high dissipation  
388 is found (figure 5). Finally, it adds more inhomogeneity to the reflected internal tide.

389 The complexity grows if other real-world influences are to be accounted for. The East Australian Current  
390 flows along this slope, varying the stratification in the horizontal, provides lateral shears that can distort the  
391 internal tide response, and carrying eddies that can add a strong time dependence to these effects. Even in  
392 two dimensions, the strength of the internal tide reflection can be significantly impacted by the phase of the  
393 incoming tide with other baroclinic modes Klymak et al. (2011) or the barotropic (Kelly and Nash 2010). The  
394 simulations here exclude the local barotropic tide, so this would certainly complicate the reflected response.  
395 Finally, the internal tide used here was monotonic, whereas the real tide will have other frequencies, most  
396 notably subinertial diurnal frequencies that will have trapped wave responses (personal communication, R.  
397 Musgrave).

398 Regardless, it is useful to have separated the “simplest” response we could in this system to tease apart the  
399 dominant physics. This response is complex enough as it is that it should be clear that solely observational  
400 efforts to balance a reflection budget are going to be a challenge. Merging simulations and observations is a  
401 likely way forward in understanding the wave field in this complex slope region.

402 With respect to the reflection problem, the modeled slope has a relatively high reflection back into the  
403 open ocean, with as much as 65% of the incoming energy being reflected as mode-1. Its possible that higher  
404 resolution runs will be more dissipative, and that stronger forcing will lead to a higher fraction of dissipation.  
405 However, these simulations, and the results from the rest of the experiment to date (i.e. Johnston et al. 2015)  
406 indicate that bulk of the energy from the Macquarie Ridge must dissipate elsewhere.

407 *Acknowledgments.*

408 Start acknowledgments here.

## REFERENCES

- <sup>411</sup> Baines, P. G., 2007: Internal tide generation by seamounts. *Deep Sea Res. I*, **54** (9), 1486 – 1508, doi:  
<sup>412</sup> <http://dx.doi.org/10.1016/j.dsr.2007.05.009>, URL <http://www.sciencedirect.com/science/article/pii/S0967063707001306>.
- <sup>414</sup> Bonod, N., E. Popov, and M. Nevière, 2005: Differential theory of diffraction by finite cylindrical objects.  
<sup>415</sup> *JOSA A*, **22** (3), 481–490.
- <sup>416</sup> Boyer, T., et al., 2013: *World Ocean Database 2013*. NOAA Atlas NESDIS 72, doi:10.7289/V5NZ85MT.
- <sup>417</sup> Brink, K., 1991: Coastal-trapped waves and wind-driven currents over the continental shelf. *Annu. Rev. Fluid Mech.*, **23**, 389–412.
- <sup>419</sup> Buijsman, M. C., et al., 2014: Three-dimensional double-ridge internal tide resonance in Luzon Strait. *J. Phys. Oceanogr.*, **44** (3), 850–869.
- <sup>421</sup> Carter, G., et al., 2008: Energetics of M 2 Barotropic-to-Baroclinic Tidal Conversion at the Hawaiian Islands.  
<sup>422</sup> *Journal of Physical Oceanography*, **38** (10), 2205–2223.
- <sup>423</sup> Dale, A. C., J. M. Huthnance, and T. J. Sherwin, 2001: Coastal-trapped waves and tides at near-inertial  
<sup>424</sup> frequencies. *J. Phys. Oceanogr.*, **31** (10), 2958–2970.
- <sup>425</sup> Dale, A. C. and T. J. Sherwin, 1996: The extension of baroclinic coastal-trapped wave theory to superinertial  
<sup>426</sup> frequencies. *J. Phys. Oceanogr.*, **26** (11), 2305–2315.
- <sup>427</sup> Johnston, T. M. S., D. L. Rudnick, and S. M. Kelly, 2015: Standing internal tides in the Tasman Sea  
<sup>428</sup> observed by gliders, doi:<http://www-pord.ucsd.edu/~shaunj/files/standing20150528.pdf>, in press *J. Phys. Oceanogr.*
- <sup>430</sup> Johnston, T. S. and M. A. Merrifield, 2003: Internal tide scattering at seamounts, ridges, and islands. *J. Geophys. Res.*, **108** (C6), 3180, doi:10.1029/2002JC01528.

- 432 Kang, D., 2011: Barotropic and baroclinic tidal energy. Ph.D. thesis, Stanford University.
- 433 Kang, D. and O. Fringer, 2012: Energetics of barotropic and baroclinic tides in the monterey bay area. *J.  
434 Phys. Oceanogr.*, **42** (2), 272–290.
- 435 Kelly, S. and J. Nash, 2010: Internal-tide generation and destruction by shoaling internal tides. *Geophysical  
436 Research Letters*, **37**, L23 611.
- 437 Kelly, S. M., N. L. Jones, and J. D. Nash, 2013a: A coupled model for laplace's tidal equations in a fluid  
438 with one horizontal dimension and variable depth. *Journal of Physical Oceanography*, (2013).
- 439 Kelly, S. M., N. L. Jones, and J. D. Nash, 2013b: A coupled model for laplace's tidal equations in a  
440 fluid with one horizontal dimension and variable depth. *Journal of Physical Oceanography*, (2013), doi:  
441 10.1175/JPO-D-12-0147.1.
- 442 Kelly, S. M., N. L. Jones, J. D. Nash, and A. F. Waterhouse, 2013c: The geography of semidiurnal mode-  
443 1 internal-tide energy loss. *Geophysical Research Letters*, n/a–n/a, doi:10.1002/grl.50872, URL <http://dx.doi.org/10.1002/grl.50872>.
- 444 Klymak, J., M. Alford, R. Pinkel, R. Lien, Y. Yang, and T. Tang, 2011: The breaking and scattering of the  
445 internal tide on a continental slope. *J. Phys. Oceanogr.*, **41**, 926–945, doi:10.1175/2010JPO4500.1.
- 446 Klymak, J. M. and S. M. Legg, 2010: A simple mixing scheme for models that resolve breaking internal  
447 waves. *Ocean Modell.*, **33** (3-4), 224 – 234, doi:10.1016/j.ocemod.2010.02.005.
- 448 Klymak, J. M., et al., 2006: An estimate of tidal energy lost to turbulence at the Hawaiian Ridge. *J. Phys.  
449 Oceanogr.*, **36**, 1148–1164.
- 450 Legg, S. and J. M. Klymak, 2008: Internal hydraulic jumps and overturning generated by tidal flow over a  
451 tall steep ridge. *J. Phys. Oceanogr.*, **38** (9), 1949–1964.
- 452 Marshall, J., E. Shuckburgh, H. Jones, and C. Hill, 2006: Estimates and implications of surface eddy  
453 diffusivity in the Southern Ocean derived from tracer transport. *J. Phys. Oceanogr.*, **36** (9), 1806–1821.

- 455 Martini, K., M. Alford, J. Nash, E. Kunze, and M. Merrifield, 2007: Diagnosing a partly standing internal  
456 wave in Mamala Bay, Oahu. *Geophys. Res. Lett.*, **34** (17), L17604.
- 457 Martini, K. I., M. H. Alford, E. Kunze, S. M. Kelly, and J. D. Nash, 2013: Internal bores and breaking  
458 internal tides on the oregon continental slope. *J. Phys. Oceanogr.*, **43**, 120–139.
- 459 Melet, A., R. Hallberg, S. Legg, and K. Polzin, 2013: Sensitivity of the ocean state to the vertical distribution  
460 of internal-tide-driven mixing. *J. Phys. Oceanogr.*, **43** (3), 602–615.
- 461 Mercier, M. J., N. B. Garnier, and T. Dauxois, 2008: Reflection and diffraction of internal waves analyzed  
462 with the Hilbert transform. *Phys. Fluids*, **20** (8), 086601.
- 463 Nash, J., M. Alford, E. Kunze, K. Martini, and S. Kelley, 2007: Hotspots of deep ocean mixing on the  
464 Oregon continental slope. *Geophys. Res. Lett.*, **34**, L01605, doi:10.1029/2006GL028170.
- 465 Nash, J. D., E. Kunze, J. M. Toole, and R. W. Schmitt, 2004: Internal tide reflection and turbulent mixing  
466 on the Continental Slope. *J. Phys. Oceanogr.*, 1117–1134.
- 467 Polzin, K. L., 2009: An abyssal recipe. *Ocean Modelling*, **30** (4), 298–309, doi:doi:10.1016/j.ocemod.2009.  
468 07.007.
- 469 Rainville, L., T. Johnston, G. S. Carter, M. A. Merrifield, R. Pinkel, P. F. Worcester, and B. D. Dushaw,  
470 2010: Interference pattern and propagation of the m2 internal tide south of the hawaiian ridge. *J. Phys.*  
471 *Oceanogr.*, **40** (2).
- 472 Smith, W. and D. Sandwell, 1997: Global sea floor topography from satellite altimetry and ship depth  
473 soundings. *Science*, **277** (5334), 1956.
- 474 St. Laurent, L. and C. Garrett, 2002: The role of internal tides in mixing the deep ocean. *J. Phys. Oceanogr.*,  
475 **32**, 2882–2899.
- 476 Whiteway, T., 2009: Australian bathymetry and topography grid, june 2009. scale 1:5000000. Tech. rep.,  
477 Geoscience Australia, Canberra. doi:10.4225/25/53D99B6581B9A.

- <sup>478</sup> Zhao, Z. and M. H. Alford, 2009: New altimetric estimates of mode-1 M2 internal tides in the central North  
<sup>479</sup> Pacific Ocean. *J. Phys. Oceanogr.*, **39** (7), 1669–1684.

## 480 List of Figures

481 1	Schematic of the difficulty of quantifying reflecting fluxes in an inhomogeneous environment.	25
482	Plane waves are trivial. Inhomogeneous incoming waves or reflections are significantly more	
483	difficult.	
484 2	Location of TTide experiment: a) Energy flux in a regional numerical simulation. Color is	
485	the absolute value of the flux, arrows it's direction. The magenta box indicates the numerical	
486	modeling domain used in this paper. b) Detail of the bathymetry on the Tasman slope. The	
487	magenta lines indicate 100 km in the x-direction, and 300 km in the y direction in the modeling	
488	domain used in this paper.	26
489 3	a) Forcing used to drive the models used in this paper. Two mode-1 internal wave sources	
490	are located to the south east (blue lines). The model domain is rotated 12 degrees from	
491	geographic so the shelf break approximately lies along $x = 0$ . Typical model domain and	
492	sponge region is indicated as green rectangles. The 250, and 3000-m isobaths are contoured.	
493	Arrows show the direction of the energy flux, and are scaled by its strength. b) Energy flux	
494	of analytical response of energy reflecting from a wall at $x = 0$ , north of $y = 0$ . c) Phase of	
495	reflected response.	27
496 4	a)–d) Surface x-direction velocity for four snapshots. a) is the initial conditions (slightly	
497	modified after a tidal cycle) and d) is the steady state. Grey contours are depths at 3000,	
498	2000, 1000, and 250-m. e)–h) is depth-integrated baroclinic energy flux at the same time	
499	periods, with arrows indicating direction.	28
500 5	Energy budget over the 19th tidal cycle of a) Barotropic to baroclinic conversion; b) Baro-	
501	clinic energy flux convergence ( $-\nabla F_{bc}$ ); c) rate of change of baroclinic energy; d) residual	
502	representing the dissipation in the model $D = -\nabla \mathbf{F}_{bc} + \text{Conv.} - dE/dt$ . The green box is the	
503	region for the energy time series (figure 6b).	29

6 a) Integral in  $x$  to 80 km offshore of the energy terms in figure 5 for the REAL case. Note  
 504 that the barotropic-baroclinic term (red) is of the same order as the baroclinic convergence  
 505 (cyan) and the residual dissipation (gray) for most of the shelf. b) Energy budget time series  
 506 for the “Real” case, tidally averaged, where time is normalized by  $T = 12.4h$ , between  $y = 0$   
 507 to  $y = 400$  km. There is still a small residual increase in the energy with time (purple),  
 508 representing the accumulation of high-mode energy in the region. Net barotropic-barocline  
 509 conversion (red) is small and negative, indicating a small net loss to the barotropic tide in  
 510 this region. The bulk of the budget is the balance between baroclinic flux convergence (blue)  
 511 and the residual “dissipation” (gray). c) Net flux in the box defined by  $0 < x < 80$  km, and  
 512  $0 < y < 400$  km. Green is the value for the net flux (no modal decomposition). Blue bars are  
 513 the modal decomposition. There is a net incoming flux in mode 1 and net reflecting fluxes in  
 514 higher modes (primarily modes 2-4).

## 516 7 Cross sections of topographies from $y = 50$ km.

517        8 Energy flux for six geometries at tidal cycle 20. Grey depth contours are -3000, -2000, -1000  
 518                  and -250 m. Arrows indicate the direction of energy flux. See figure 7 for bathymetry cross  
 519                  sections at  $y = 50$  km.

520 9 Mode-1 decomposition of energy fluxes for the SHELF experiment. a) Incoming energy flux  
521 calculated from the NO TOPO simulation (figure 8a). Note that the shelf bathymetry is  
522 contoured on this plot (grey lines, and green “land”), but this bathymetry was not part  
523 of this simulation. The green line demarks the region the energy budget in the inset was  
524 integrated over. The green diamonds are the location of a synthetic mooring, and the arrow  
525 indicates the estimated incoming flux from a plane wave fit over the three moorings of the  
526 “Total” simulation (see text). b) Reflected energy flux calculated from the difference between  
527 the velocities and displacements of the Total simulation (panel d) and the “Incoming” (panel  
528 a). Blue arrow is the outgoing flux from a plane wave fit over the mooring array from the  
529 “Total” simulation. c) Energy flux cross terms between the incoming and outgoing waves. d)  
530 Total simulation from the SHELF case (figure 8d)

531	10	Mode-1 decomposition of energy fluxes for the RISE-SHELF experiment.	34
532	11	Energy decomposition based on taking the No TOPO case as the incoming wave, and RISE	
533		as the total wavefield and looking at the energy flux of the difference between their waves	
534		(reflected wave field) and the energy flux associated with the cross terms between.	35
535	12	a) Energy budget from 80 km by 80 km control volumes along the continental slope from the	
536		REAL simulations. The incoming flux (red) is compared to the reflected (blue) and the cross	
537		terms (purple). b) The reflection co-efficients. The blue line is $R_1$ , the mode-1 reflectivity in	
538		the 80-km control volumes along slope. The black line is the mode-1 reflectivity from a linear	
539		model (?), and the grey lines behind are the cumulative sum of modes 2, to 5 and then all	
540		the modes. These do not sum up to one because the linear model has some “viscosity” that	
541		removes some high-mode energy. The dashed lines are the mean of $R_1$ from the linear model	
542		if a constant average is taken (light blue, dashed), and if weighted by the diffracted beam	
543		strength (purple, dashed).	36
544	13	Barotropic to baroclinic conversion for different shelf widths from widest (a) to narrowest (d).	
545		Arrows are barotropic flux vectors. Note how the along-slope barotropic flux is almost entirely	
546		confined to conversion dipoles along slope.	37

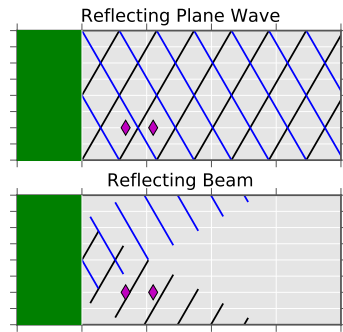


FIG. 1. Schematic of the difficulty of quantifying reflecting fluxes in an inhomogeneous environment. Plane waves are trivial. Inhomogeneous incoming waves or reflections are significantly more difficult.

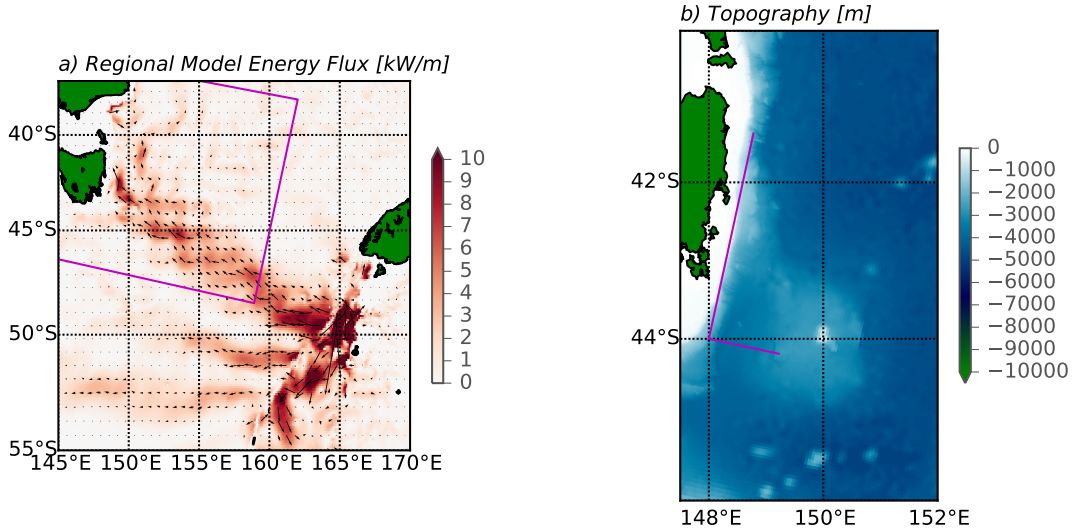


FIG. 2. Location of TTide experiment: a) Energy flux in a regional numerical simulation. Color is the absolute value of the flux, arrows its direction. The magenta box indicates the numerical modeling domain used in this paper. b) Detail of the bathymetry on the Tasman slope. The magenta lines indicate 100 km in the x-direction, and 300 km in the y direction in the modeling domain used in this paper.

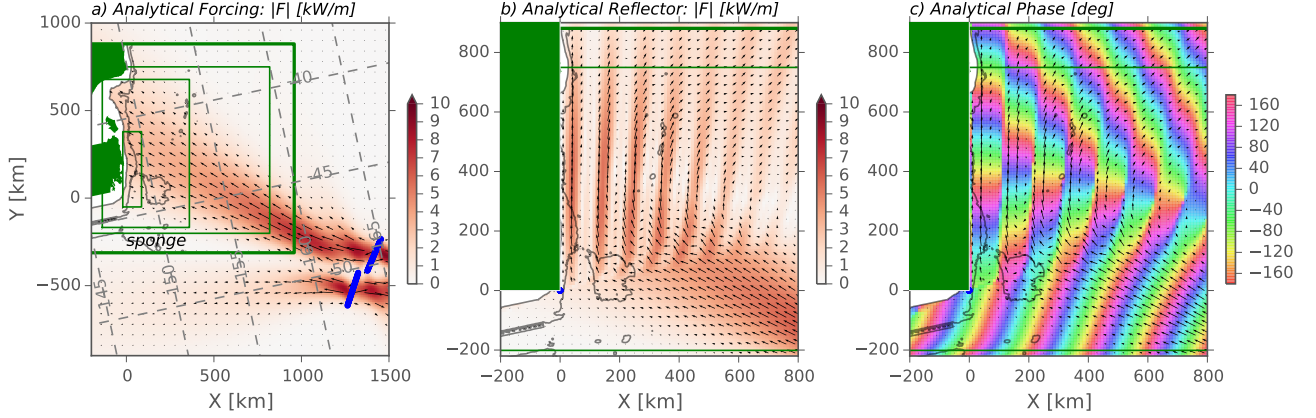


FIG. 3. a) Forcing used to drive the models used in this paper. Two mode-1 internal wave sources are located to the south east (blue lines). The model domain is rotated 12 degrees from geographic so the shelf break approximately lies along  $x = 0$ . Typical model domain and sponge region is indicated as green rectangles. The 250, and 3000-m isobaths are contoured. Arrows show the direction of the energy flux, and are scaled by its strength. b) Energy flux of analytical response of energy reflecting from a wall at  $x = 0$ , north of  $y = 0$ . c) Phase of reflected response.

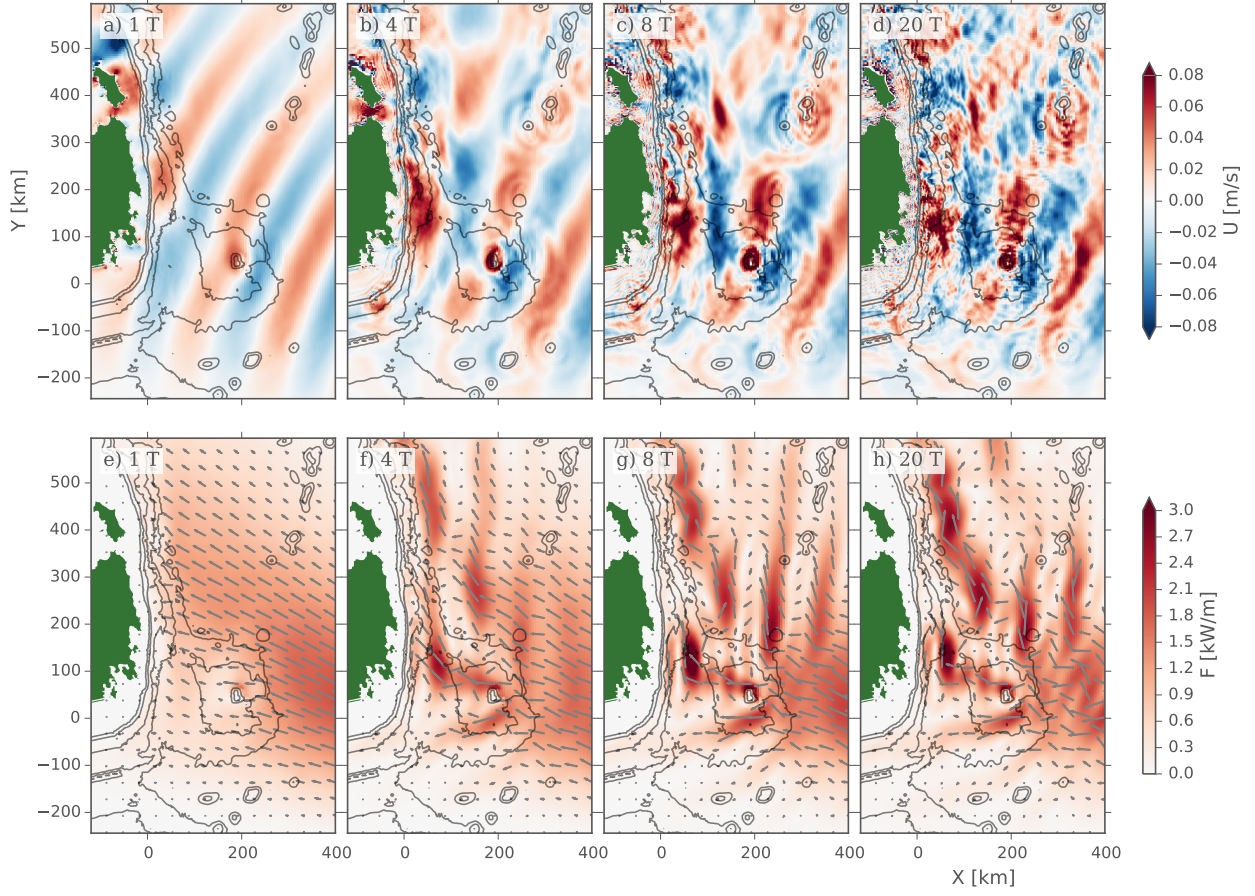


FIG. 4. a)-d) Surface x-direction velocity for four snapshots. a) is the initial conditions (slightly modified after a tidal cycle) and d) is the steady state. Grey contours are depths at 3000, 2000, 1000, and 250-m. e)-h) is depth-integrated baroclinic energy flux at the same time periods, with arrows indicating direction.

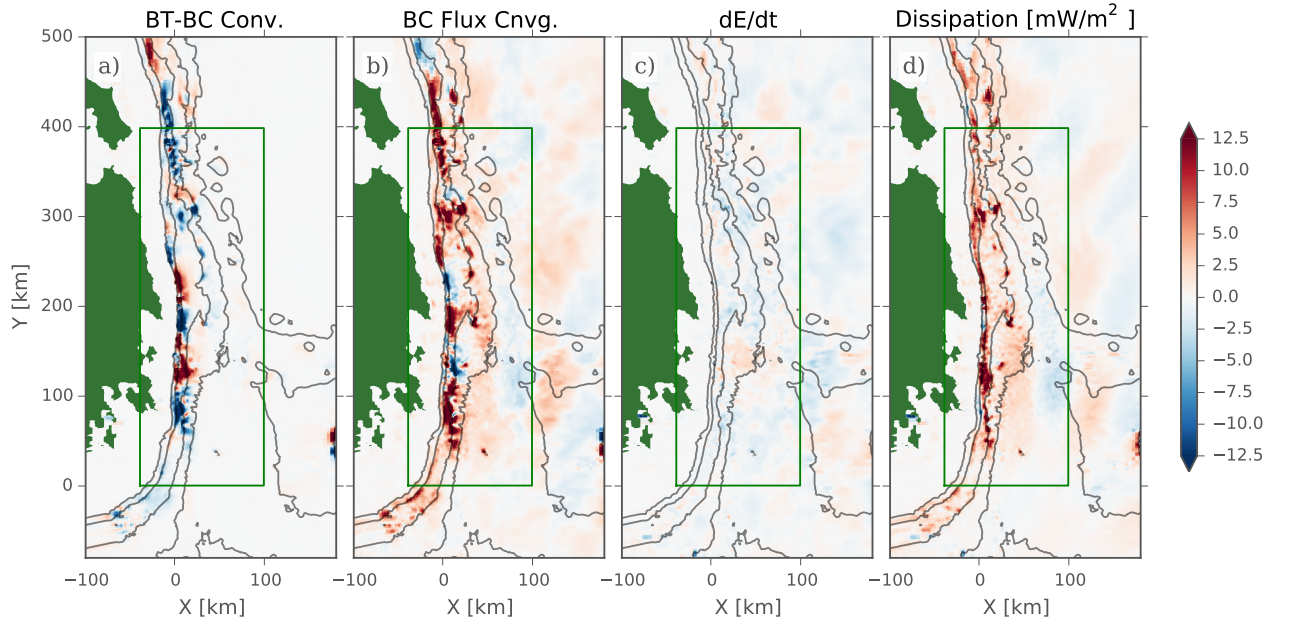


FIG. 5. Energy budget over the 19th tidal cycle of a) Barotropic to baroclinic conversion; b) Baroclinic energy flux convergence ( $-\nabla F_{bc}$ ); c) rate of change of baroclinic energy; d) residual representing the dissipation in the model  $D = -\nabla F_{bc} + \text{Conv.} - dE/dt$ . The green box is the region for the energy time series (FIG. 6b).

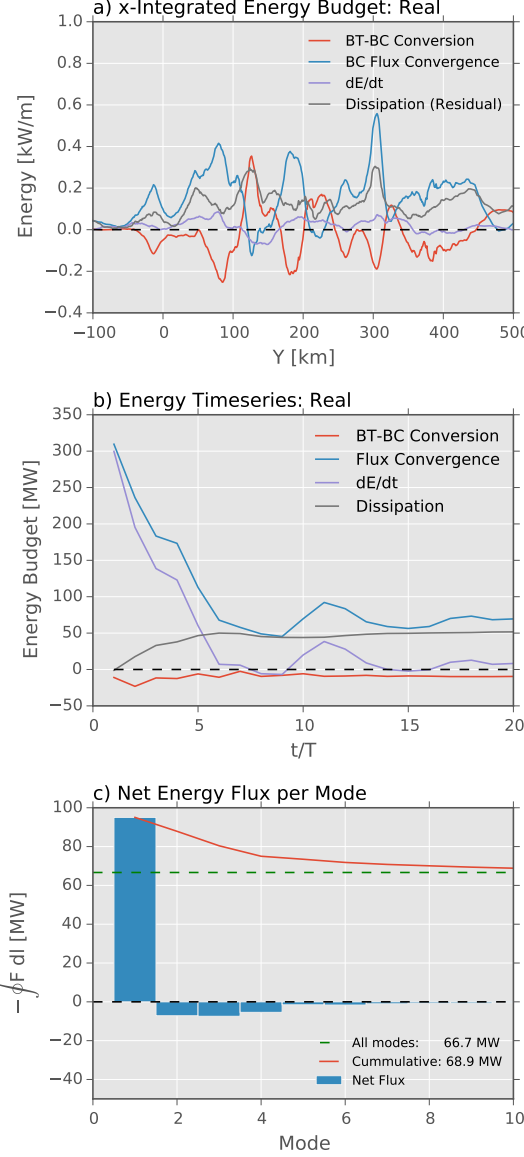


FIG. 6. a) Integral in  $x$  to 80 km offshore of the energy terms in FIG. 5 for the REAL case. Note that the barotropic-baroclinic term (red) is of the same order as the baroclinic convergence (cyan) and the residual dissipation (gray) for most of the shelf. b) Energy budget time series for the “Real” case, tidally averaged, where time is normalized by  $T = 12.4h$ , between  $y = 0$  to  $y = 400$  km. There is still a small residual increase in the energy with time (purple), representing the accumulation of high-mode energy in the region. Net barotropic-baroclinic conversion (red) is small and negative, indicating a small net loss to the barotropic tide in this region. The bulk of the budget is the balance between baroclinic flux convergence (blue) and the residual “dissipation” (gray). c) Net flux in the box defined by  $0 < x < 80$  km, and  $0 < y < 400$  km. Green is the value for the net flux (no modal decomposition). Blue bars are the modal decomposition. There is a net incoming flux in mode 1 and net reflecting fluxes in higher modes (primarily modes 2-4).

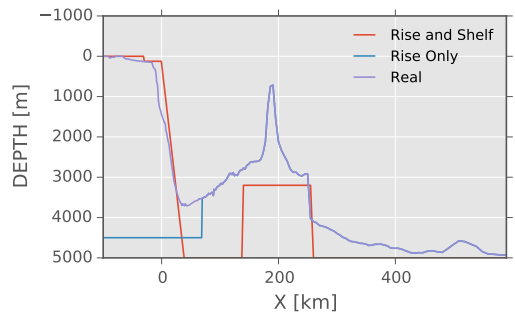


FIG. 7. Cross sections of topographies from  $y = 50$  km.

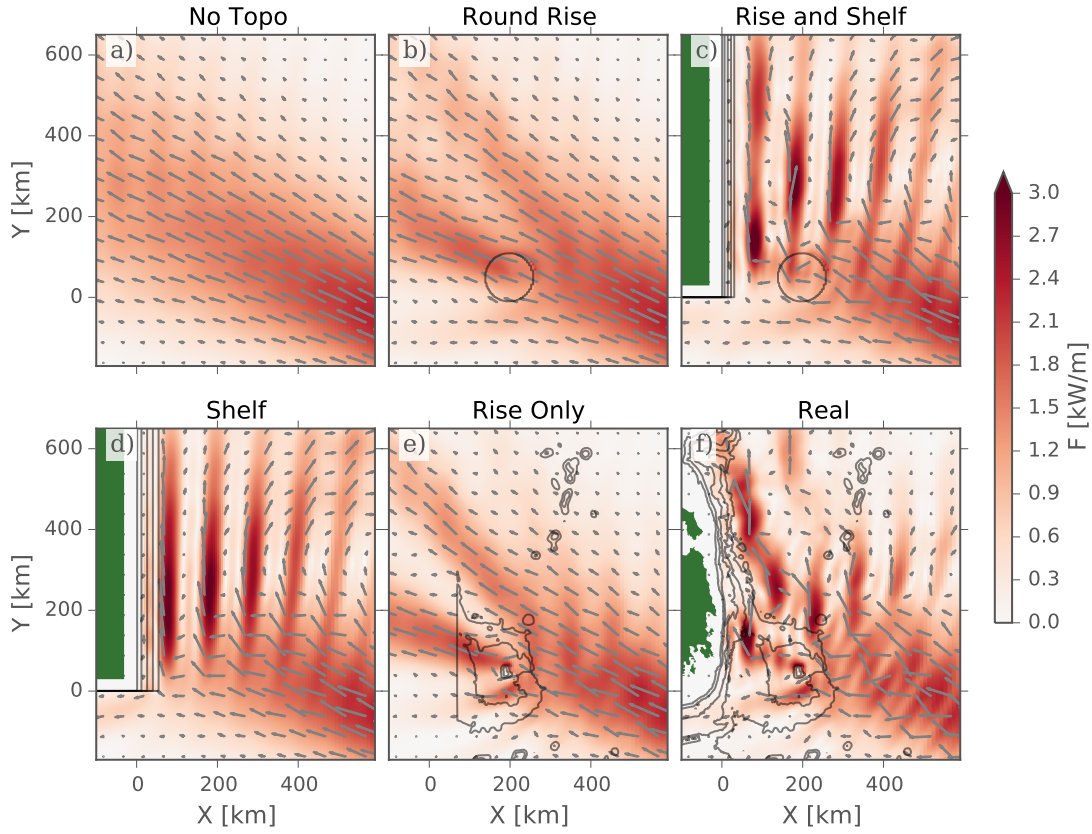


FIG. 8. Energy flux for six geometries at tidal cycle 20. Grey depth contours are -3000, -2000, -1000 and -250 m. Arrows indicate the direction of energy flux. See FIG. 7 for bathymetry cross sections at  $y = 50$  km.

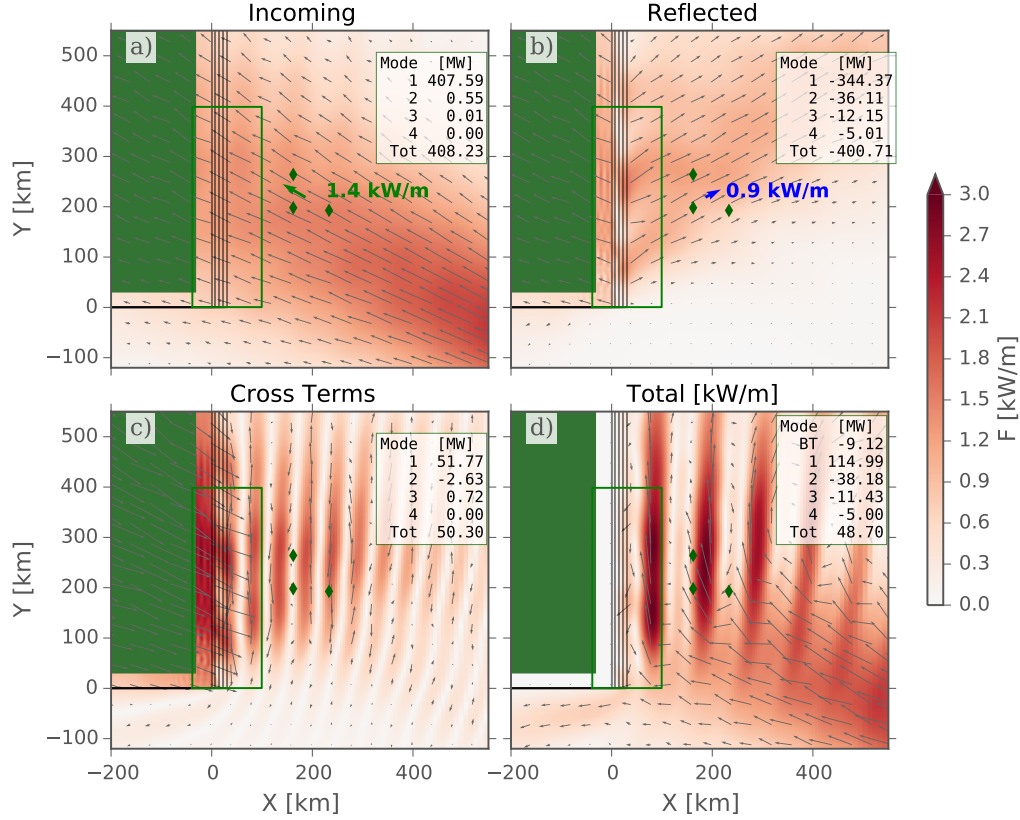


FIG. 9. Mode-1 decomposition of energy fluxes for the SHELF experiment. a) Incoming energy flux calculated from the NO TOPO simulation (FIG. 8a). Note that the shelf bathymetry is contoured on this plot (grey lines, and green “land”), but this bathymetry was not part of this simulation. The green line marks the region the energy budget in the inset was integrated over. The green diamonds are the location of a synthetic mooring, and the arrow indicates the estimated incoming flux from a plane wave fit over the three moorings of the “Total” simulation (see text). b) Reflected energy flux calculated from the difference between the velocities and displacements of the Total simulation (panel d) and the “Incoming” (panel a). Blue arrow is the outgoing flux from a plane wave fit over the mooring array from the “Total” simulation. c) Energy flux cross terms between the incoming and outgoing waves. d) Total simulation from the SHELF case (FIG. 8d)

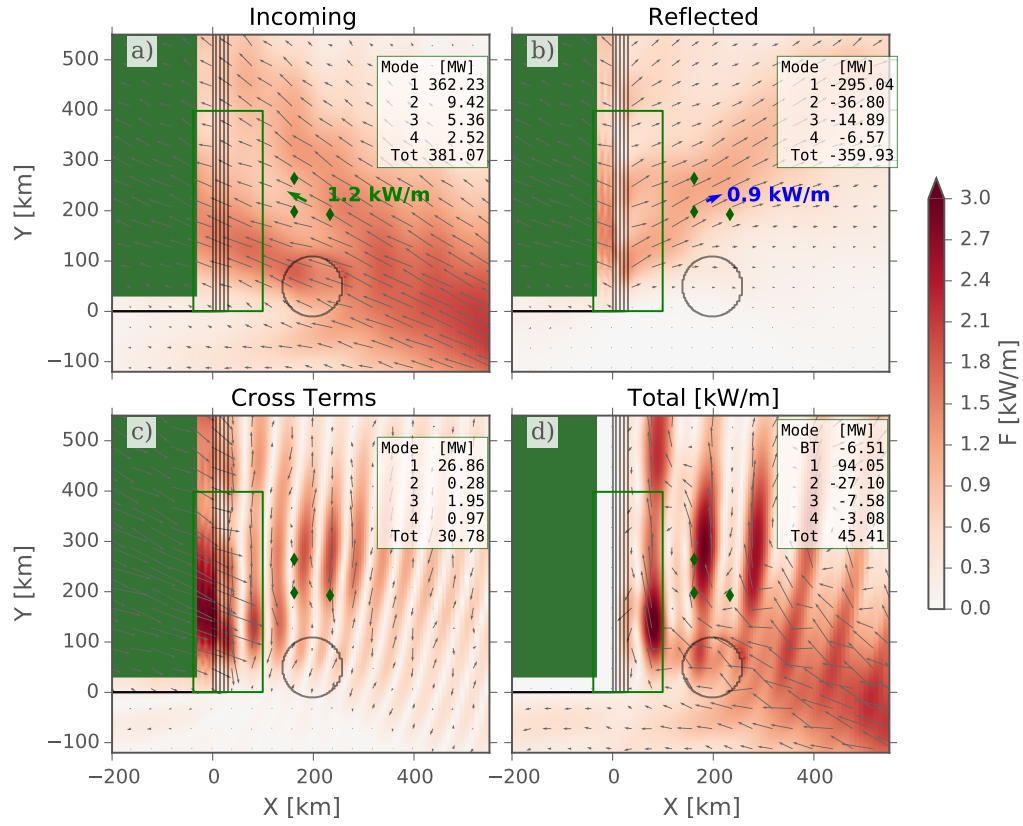


FIG. 10. Mode-1 decomposition of energy fluxes for the RISE-SHELF experiment.

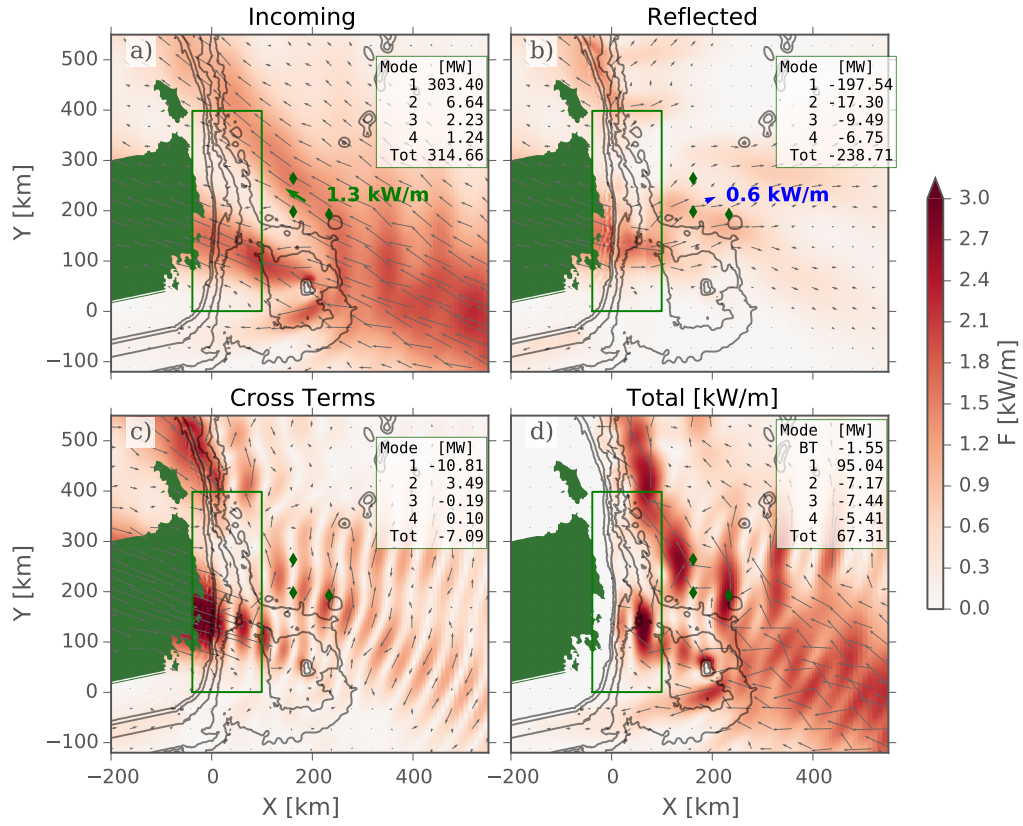


FIG. 11. Energy decomposition based on taking the No TOPO case as the incoming wave, and RISE as the total wavefield and looking at the energy flux of the difference between their waves (reflected wave field) and the energy flux associated with the cross terms between.

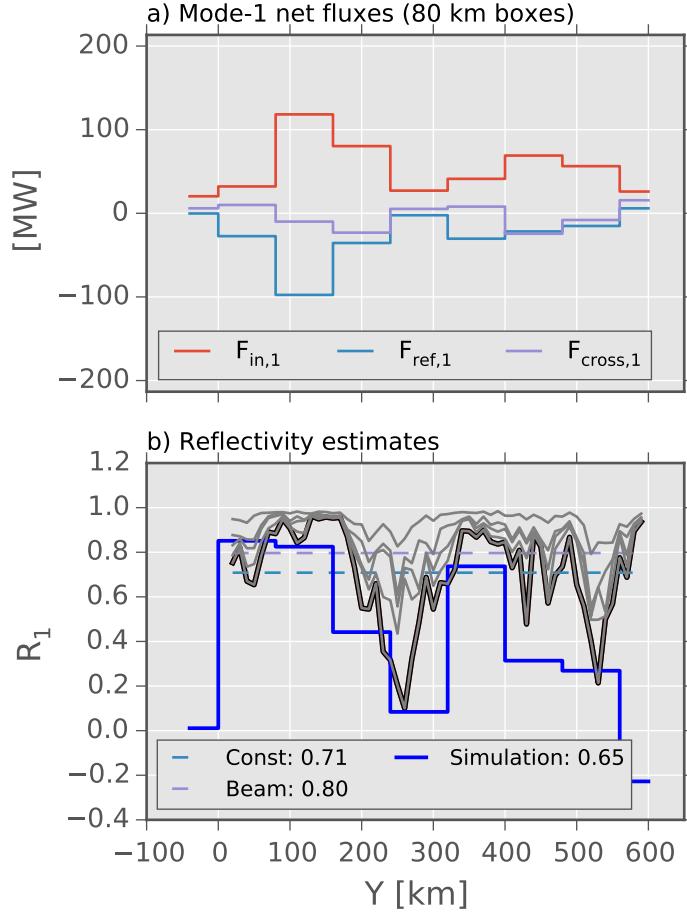


FIG. 12. a) Energy budget from 80 km by 80 km control volumes along the continental slope from the REAL simulations. The incoming flux (red) is compared to the reflected (blue) and the cross terms (purple). b) The reflection co-efficients. The blue line is  $R_1$ , the mode-1 reflectivity in the 80-km control volumes along slope. The black line is the mode-1 reflectivity from a linear model (?), and the grey lines behind are the cumulative sum of modes 2, to 5 and then all the modes. These do not sum up to one because the linear model has some “viscosity” that removes some high-mode energy. The dashed lines are the mean of  $R_1$  from the linear model if a constant average is taken (light blue, dashed), and if weighted by the diffracted beam strength (purple, dashed).

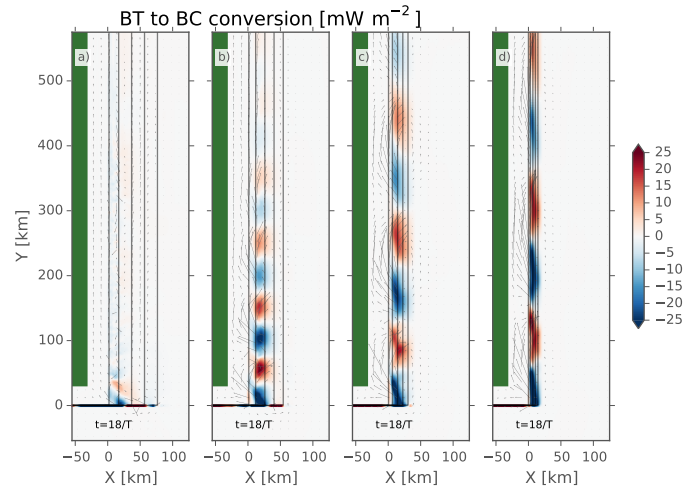


FIG. 13. Barotropic to baroclinic conversion for different shelf widths from widest (a) to narrowest (d). Arrows are barotropic flux vectors. Note how the along-slope barotropic flux is almost entirely confined to conversion dipoles along slope.